Soft Matter

PAPER

View Article Online
View Journal | View Issue

Cite this: *Soft Matter*, 2024, **20**, 7946

Controlling the roll-to-helix transformation in electron-beam-patterned gel-based micro-ribbons†

Xinpei Wu,[a] Teng Zhang [b] and Matthew Libera *[a]

Received 1st June 2024,
Accepted 20th September 2024

DOI: 10.1039/d4sm00666f

rsc.li/soft-matter-journal

Helix formation has been of ongoing interest because of its role in both natural and synthetic materials systems. It has been extensively studied in gel-based ribbons where swelling anisotropies drive out-of-plane bending. In contrast to approaches based on photolithography or mechanical bilayer construction, we use electron-beam patterning to create microscale ribbons at ~1–100 μm length scales in pure homopolymer precursor films of poly(acrylic acid) (PAA). The radiation chemistry creates a ribbon comprising a crosslinked hydrophobic top layer and a hydrophilic gel bottom layer with a continuous through-thickness variation in between. The classic roll-to-helix transition occurs as the ribbon aspect ratio increases. Notably, we see examples of single-loop rolls, multi-loop rolls, minimal-pitch helices, plus a transition structure comprising both helical and roll-like features. Finite-element modelling recapitulates key aspects of these conformations. Increasing the pH from below to above the PAA pK_a increases the out-of-plane bending to the extent that the ribbons plastically deform and nonminimal-pitch helices form across a wide range of aspect ratios and irradiation conditions. The nonminimal pitch is caused by an in-plane anisotropy associated with the plastic deformation. We mimic this anisotropy by patterning ribbons comprising micro-tiles separated by gaps which receive electron exposure due to proximity effects. We observe a transition from roll to helix to tube with increasing gap angle. The chirality is completely determined by the gap orientation ($\pm\theta$). However, in contrast to established approaches to generate in-plane anisotropies based on mechanical properties, finite-element modelling indicates that anisotropic through-thickness swelling of the gap material plays a dominant role in helix formation and suggests that this micro-composite ribbon behaves like a rigid origami metamaterial where deformation at the creases (the gaps) between structural elements controls the shape shifting.

1. Introduction

Helix formation has been a subject of longstanding interest to the scientific community. Helices of various forms are found throughout nature in such diverse situations as plant tendrils,[1] animal horns and seashells,[2,3] and, at a very different length scale, the tertiary structure of proteins and poly(nucleic acids).[4,5] Helical geometries have likewise been exploited in an array of engineering applications including mechanical systems (*e.g.*, gears, screws), synthetic helical polymers and supramolecular assemblies,[6] and artificial muscles and actuation systems,[7,8] among others. In parallel, there has been broad interest in using various fabrication methods to generate combinations of in-plane and out-of-plane stresses, together with geometric constraints, that drive shape-shifting processes able to convert a thin and flat ribbon into a 3D helix. This effort has provided significant insight into the mechanics of helix formation and helped lay an important foundation for the design and synthesis of stimuli-responsive shape-shifting structures with more complex geometries.[9,10]

The conventional ribbon-to-helix shape-shifting geometry comprises a ribbon with length L, width W, and thickness h. Typically, h is much smaller than both W and L, and the aspect ratio of L/W is typically $\gg 1$. A stress gradient through the ribbon thickness introduces a mechanical asymmetry that can drive a shape change in response to external stimuli. The classic example is the thermal expansion of a bilayer metallic strip whose use dates back centuries[11] and whose behavior was first modelled by Timoshenko in 1925.[12] More recent approaches have constructed rubber bilayers with one or both layers prestressed,[13–15] inorganic lattice-mismatched bilayer

[a] *Department of Chemical Engineering and Materials Science, Stevens Institute of Technology, Hoboken, NJ, USA. E-mail: mlibera@stevens.edu*
[b] *Department of Mechanical and Aerospace Engineering, Syracuse University, Syracuse, NY, USA*

† Electronic supplementary information (ESI) available. See DOI: https://doi.org/10.1039/d4sm00666f

thin films,[16] and hydrogel ribbons produced by photolithography where light adsorption creates a through-thickness gradient in crosslink density.[17] Stress gradients produce an out-of-plane bending moment which forces the ribbon to curl. If the curvature is large enough and the ribbon is long enough, the curl will complete a full circle. For longer lengths, the curl will either form a roll or a helix depending on which conformation has the lower energy. For a roll, each subsequent layer has an incrementally different radius, so the bending energy varies. For a helix, the radius is preserved but the roll shears laterally so that each sequential turn avoids the previous one, and there is thus an increase in the shear energy. The ribbon width plays an important role, because it influences the self-avoiding condition needed for helix formation. Wider ribbons favor a roll conformation, while smaller widths favor a helical conformation.

In addition to the out-of-plane bending caused by a through thickness anisotropy, anisotropy within the ribbon plane further influences helix formation. In the absence of a through-thickness anisotropy, in-plane anisotropy by itself can cause bending and helix formation.[18] In-plane anisotropy can furthermore convert a helix from one with a minimal pitch that just satisfies the self-avoiding condition to one with a non-minimal pitch where there are gaps between subsequent turns of the helix. These two conformations are differentiated by the angle of the in-plane anisotropy relative to the principal axis of the helix. Such in-plane anisotropies occur naturally in seed pods and other plant systems[13] and have been created in synthetic systems by extrinsically incorporating high-modulus wires or fibers in bilayer systems[19] or by extrinsically patterning lines with different mechanical properties in a ribbon.[18,20]

In contrast to prior approaches to fabricate shape-shifting ribbons using photolithography or by mechanical construction, we have recently introduced electron-beam patterning as a means to create microscale helices.[21] E-beam lithography is well known for its ability to flexibly create different patterns without a mask and achieve nanoscale spatial resolution.[22] Somewhat less appreciated is the fact that electrons can drive various chemical processes such as crosslinking in homopolymers without more complex resist formulations that include multifunctional crosslinkers and initiators. One classic homopolymer e-beam system is polystyrene, which preferentially crosslinks in response to electron radiation and can be used as a negative resist.[23] We and others have shown that poly(ethylene glycol) [PEG] behaves similarly.[24,25] PEG thin films can be converted into e-beam patterned microgels grafted onto the surface of an underlying hard surface and control surface interactions with proteins and cells as well as spatially localize various site-specific chemical reactions.[26] Poly(acrylic acid) [PAA] likewise preferentially crosslinks when exposed to energetic electrons.[21,27] Our recent work[21] patterned narrow lines, hundreds of nanometers wide and tens of microns long, in PAA films. Because of their large L/W ratio, these lines all shape-shifted into helices.

Here we expand the study of e-beam patterned PAA from one-dimensional lines to two-dimensional ribbons with widths on the order of microns. This increase in dimensionality introduces new dynamics and new control mechanisms relative to 1D lines where shape shifting was confined to helices. Wider ribbons allow for combinations of geometric parameters and pH to control shape shifting, and we show that these together can create a range of structures and responsive behaviors, some of which are quite new. Importantly, despite the fact that we use a different fabrication approach and address a different (*i.e.*, micron) length scale, the patterned ribbons follow the anticipated roll-to-helix transition as the L/W ratio increases as has been observed in other systems at larger length scales. Hence, the e-beam-patterned PAA system appears to be well-behaved in the context of what is generally known about helix formation. We show that the shape shifting in e-beam patterned PAA ribbons is driven by through-thickness gradients in the ribbon mechanical properties and swelling behavior. Significantly, and in contrast to other ribbon-fabrication methods, the e-beam approach can control the ribbon mechanical properties. We exploit that unique capability to show that the specific nature of the roll-to-helix transition can be controlled by the incident electron dose. Higher doses preserve the roll conformation because the increased radiation creates a through-thickness structure with greater rigidity, less out-of-plane curvature, and less bending energy. Lower doses and high L/W ratios create helices with a minimal pitch that satisfies the self-avoiding condition.

PAA is a weak polyelectrolyte, and increasing the pH from below to above its pK_a generates substantially higher out-of-plane bending and stabilizes the helical conformation. However, we show that increasing pH produces helices with non-minimal pitches. This occurs because of an additional in-plane anisotropy which we show is a consequence of plastic elongation within the ribbon. In contrast to established mechanisms that extrinsically generate in-plane anisotropies during ribbon fabrication, we show that the anisotropic deformation of PAA ribbons is generated intrinsically in response to a pH change. That said, we can exploit the maskless patterning flexibility of the e-beam approach to also impose an extrinsic in-plane anisotropy. We do this by patterning a novel micro-tiled ribbon structure with higher modulus tiles separated by narrow nanoscale gaps comprising high-swelling lower modulus PAA gel. With no need for a mask, we are able to pattern these gaps over a range of in-plane angles. The tiled ribbons display the classic morphological variation from ribbon to helix to tube with increasing angle. The chirality is entirely determined by the direction of the gap ($\pm\theta$). Finite-element modelling indicates that the through-thickness swelling of the gap material control the shape shifting suggesting that these tiled ribbons behave like rigid origami structures.

2. Materials and methods

The experimental methods and finite-element modelling follow procedures much like those we used previously to pattern one-dimensional lines in PAA.[21] Important elements of the procedures

are embedded here in our Results and Discussion. A detailed description is provided as ESI.†

3. Results and discussion

3.1 Electron-beam patterning of ribbons

Ribbons with an initial width W_0 (typically ~1–5 μm) and initial length L_0 (typically ~5–100 μm) were e-beam patterned in films, approximately 500 nm thick or more, of Cy3-labeled homopolymer PAA (M_w = 450 kDa) spin cast from methanol solutions onto silanized polished silicon substrates. A focused electron beam incident along the $\hat{z}$ direction was digitally rastered in the $\hat{x}$ and $\hat{y}$ directions with interpixel spacings of $\delta_x = \delta_y = 4.8$ nm. Each pixel was irradiated with a point dose of D_p (*e.g.*, 0.5 fC) using electrons with an incident energy E_0 of 2 keV or 10 keV. 2 keV electrons drive radiation chemistry in the near-surface regions of the film without reaching the substrate. 10 keV electrons can traverse the entire thickness and drive radiation chemistry both in the film and at the film/substrate interface where polymer becomes grafted to the substrate. We exploited this difference to create PAA ribbons using 2 keV electrons which were tethered at one end to a so-called tethering pad patterned using 10 keV electrons (Fig. 1(A)). After patterning, developing in an aqueous buffer removes unexposed polymer and leaves a hydrated ribbon which is tethered to the substrate but otherwise free to adopt an equilibrium shape.

Shape changes occur in part because of a through-thickness swelling gradient caused by the depth-dependent radiation chemistry. As the incident electrons penetrate the polymer film, they lose energy by a variety of inelastic scattering processes, and the electron intensity follows a Beer–Lambert type exponential decay.[28] In the case of PAA, the inelastic scattering produces radiation chemistries that lead to crosslinking and mass loss. Winzor *et al.*[29,30] have measured a G_x value – the number of crosslinking events per 100 eV of deposited energy – of 0.44 while the G value for chain scission, G_s, is close to zero. Hence, radiation-driven crosslinking is far more likely than chain scission. Mass loss occurs by the release of CO and CO_2 due to the radiation effects on the PAA acid group. The G value for damaging the acid group is $G_{COOH} = G_{CO_2} + G_{CO} = 12$.[29,30] Acid-like monomers are converted into ethylene-like monomers. We have modelled[21] the depth-dependent structure of e-beam patterned lines of PAA by combining Monte Carlo

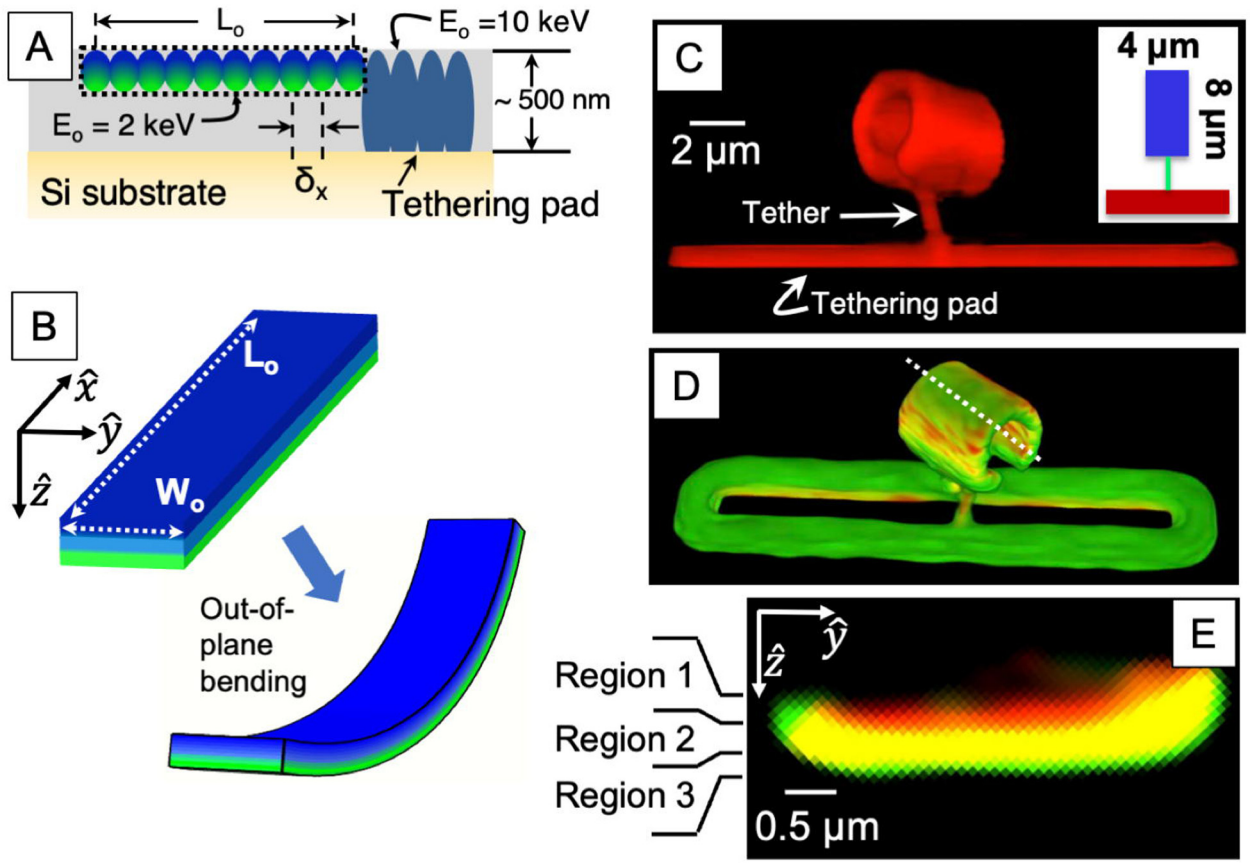

Fig. 1 (A) Schematic cross section view of the patterning geometry; (B) a patterned ribbon with lateral dimensions $W_0 \times L_0$ develops a through-thickness swelling gradient that creates out-of-plane bending; (C) confocal fluorescence imaging in pH 3.0 buffer shows that a patterned ribbon shape shifts into a single-loop roll (D_p = 0.5 fC); (D) post-patterning labelling with FITC (green) indicates the high-swelling gel regions of the pattern; (E) 2-color imaging confirms the through-thickness gradient structure that varies from highly crosslinked material at the ribbon's top surface (region 1) to high-swelling pH-responsive gel at the bottom surface (region 3).

simulations of electron trajectories and energy deposition,[31,32] radiation chemistry based on the Winzor G values,[29,30] and a model of polyelectrolyte swelling developed by Jia and Muthukumar.[33] For a range of relevant electron doses, this model indicates that the near-surface material is heavily crosslinked and does not swell. Since G_{COOH}/G_x = 27, the model furthermore predicts that all the acid groups in this region have been destroyed, and the material is essentially a highly crosslinked and hydrophobic hydrocarbon. We refer to this top portion of the ribbon as region 1 (dark blue in Fig. 1(B)). The bottom surface of the patterned ribbon (green in Fig. 1(B)), on the other hand, has a structure where, on average, each PAA molecule has undergone only one or just a few crosslinking events. Because of the high PAA molecular weight, only a small fraction of the available acid groups is damaged, and the material at the bottom surface thus behaves as a high-swelling polyelectrolyte hydrogel. We refer to this bottom portion of the ribbon as region 3. In between these extremes, the region 2 material (light blue in Fig. 1(B)) varies nonlinearly from hydrophobic and non-swelling to hydrophilic and high swelling. While for convenience we parse the ribbon into these three layers, the structural changes from the top to the bottom of the ribbon are continuous and nonlinear rather than discrete. When hydrated, the high-swelling region creates an out-of-plane bending stress (Fig. 1(B)).

Fluorescence imaging confirms the varying structure through the film thickness. We patterned a ribbon with W_0 = 4 μm and L_0 = 8 μm using D_p = 0.5 fC. This ribbon was connected to the underlying tethering pad by a so-called tethering line (tether) comprising an 8 μm segment patterned (2 keV) with a D_p = 100 fC connected to the tethering pad and a 2 μm segment with D_p = 4 fC connected to the ribbon. The overall pattern was developed in low-ionic strength phosphate buffer (pH 3.0), and then imaged the resulting (fully hydrated) structure by confocal fluorescence microscopy. Fig. 1(C) indicates that the flat rectangular plate shape shifts into a roll. Importantly, the red (Cy3) signal comes primarily from the non-swelling regions of the ribbon where the fluorophore concentration is high. The Cy3 concentration in the lightly crosslinked and high swelling region 3 is undetectably low. The high-swelling region can be visualized by post-labelling using a carbodiimide chemistry to bind amine-functionalized FITC to acid groups on the developed PAA pattern. The two-color image of Fig. 1(D) shows green intensity that indicates high-swelling gel. A section (inverted relative to Fig. 1(D)) through the roll from the location indicated by the dashed white line is shown in Fig. 1(E) and experimentally confirms the general cross-sectional ribbon structure with red intensity concentrated at the top (non-swelling region 1), green intensity at the bottom (high-swelling region 3), and the transition region 2 in between

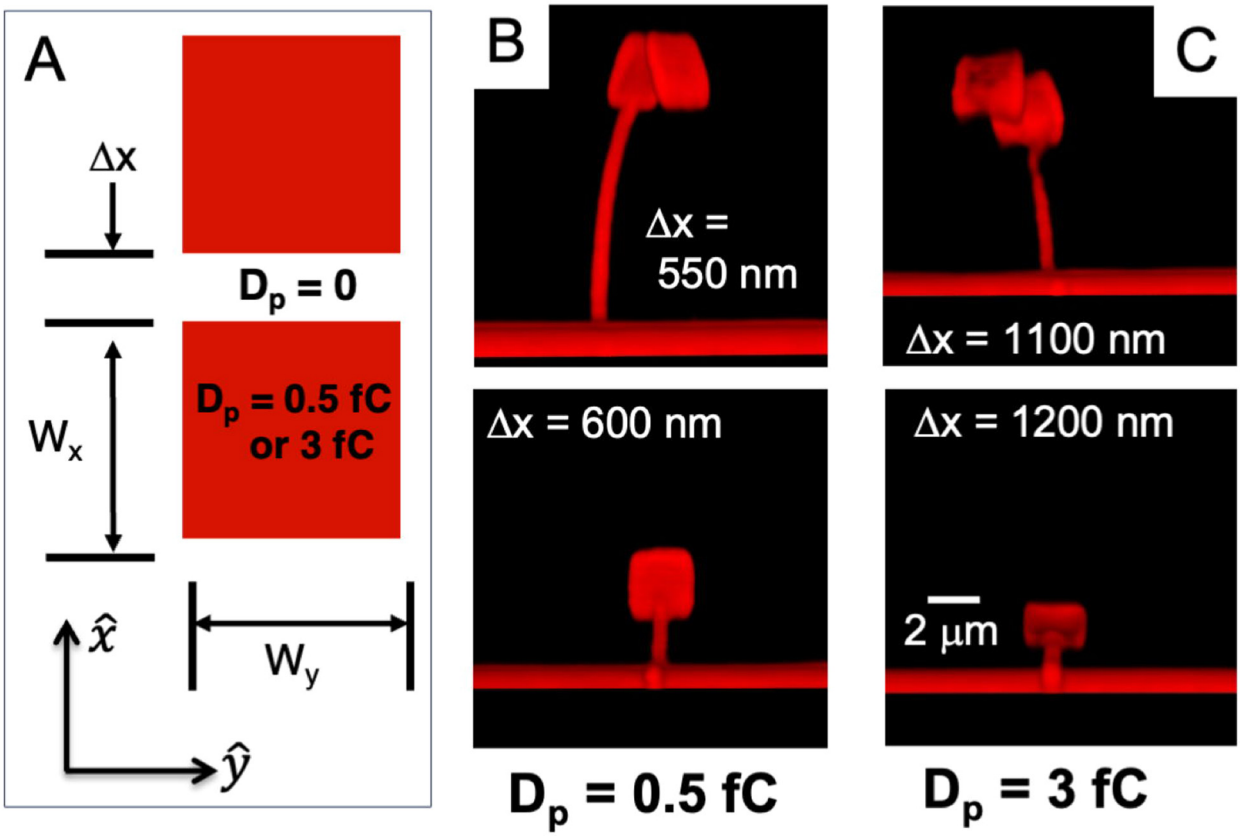

Fig. 2 A tile-separation experiment to determine the extent of lateral crosslinking due to proximity effects. (A) A top-view schematic of the experiment; (B) and (C) confocal images of hydrated patterns (0.01 M pH 3.0 buffer) with D_p = 0.5 fC and 3.0 fC, respectively. The top images show two connected tiles, while the bottom images show only the one tile tethered to the substrate.

(yellow). We note that Fig. 1(E) shows slight lateral curvature due to the region 3 swelling in the $\hat{y}$ direction. And, while our focus is not on the tethering pad, we note that the band of dark contrast there corresponds to material that is so heavily damaged by 10 keV electrons that both the pre-labelled Cy3 fluorophores and the acid groups needed for FITC post labelling were destroyed. The green contrast surrounding the tethering pad is due to high-swelling gel created by proximity effects[34] during patterning of the tethering pad.

3.2 Proximity effects

Without two-color imaging, we see no contrast in the proximity-effect regions because the Cy3 fluorophore concentration is orders of magnitude lower there than that in the area directly scribed by the incident electron beam. However, post-labelling with amine-FITC changes the properties of a shape-shifted structure. We thus instead measured the extent of the proximity effect by patterning tiles separated from each other by controllable distances and determining the critical separation where adjacent tiles became unconnected.

Proximity effects are well known.[35] They create exposure outside the patterned area. To experimentally assess their lateral extent, we patterned two adjacent tiles separated by a distance Δx and determined the critical separation beyond which the second tile would no longer be covalently bound to the first. Fig. 2(A) illustrates the patterning geometry. The two tiles had lateral dimensions of $W_x = W_y = 2$ μm. The first tile was tethered to the substrate, and the second tile was separated from the first by a gap of Δx. The gap region received no direct patterning. Exposure within the gap region was due entirely to proximity effects coming from patterning the two tiles. One set of experiments patterned the tiles with a point dose of D_p = 0.5 fC. A second set used D_p = 3.0 fC. Fig. S1 and S2 (ESI†) show confocal images for each of these experiments where Δx was varied from 300–600 nm and from 500–1200 nm, respectively. The key subset of these image sets is shown in Fig. 2(B) and (C). The top images each show two tiles. The overall structure bends because of the asymmetric through-thickness swelling in the gap region (see Section 3.6). The lower images show only one tile. The second tile was patterned, but it was unattached to the first and was washed away during the development step. We can conclude that, for the e-beam patterning conditions used in these experiments, there is a critical separation of 550 nm for D_p = 0.5 fC and 1100 nm for D_p = 3.0 fC.

3.3 Roll-to-helix transition

3.3.A Effect of the L_0/W_0 ratio. We explored the effects of ribbon geometry by varying the L_0/W_0 ratio. Fig. 3 shows one example for D_p = 0.5 fC where the hydrated ribbon thickness was ~600 nm (Fig. 1(E)). W_0 = 2 μm, and the ribbon length was varied. Fig. 3(A)–(D) show the cases where L_0 = 20, 40, 50, and 60 μm, respectively. The ribbons were developed and imaged in pH 3.0 buffer. This series of images displays the anticipated transition from roll to helix as L_0/W_0 increases. We also observe an intermediate conformation, which we refer to as a transition

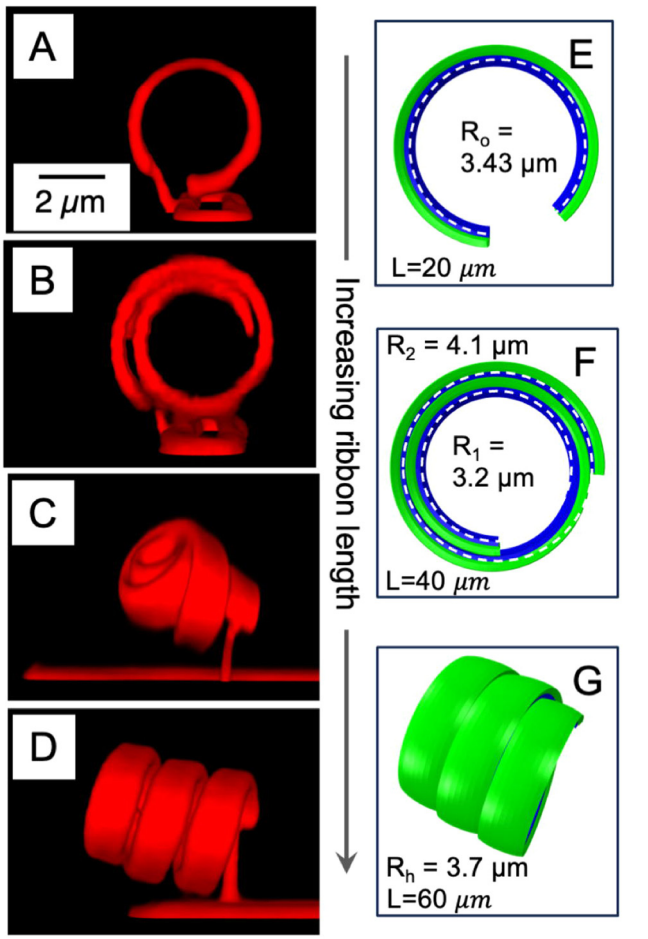

Fig. 3 Increasing the ribbon length changes the shape-shifted morphology from: (A) a roll with less than one full loop; (B) a multi-loop roll; (C) a transition structure; and (D) a minimal-pitch helix. W_0 = 2 μm; L_0 = 20, 40, 50, 60 μm, respectively; D_p = 0.5 fC. Developed and imaged in low-ionic-strength phosphate buffer (pH 3.0). Modelling (E)–(G) indicates similar trends.

structure (Fig. 3(C)), between the multi-loop roll conformation (Fig. 3(B)) and the helix conformation (Fig. 3(D)).

We measured the loop and helical radii from a series of ribbons whose lengths varied from L_0 = 8 μm to L_0 = 60 μm. The images are presented in Fig. S3 (ESI†), and the measurements are presented in Table 1. Ribbons too short to form a complete loop (L_0 = 8 and 12 μm) had the same radius (R_0 = 3.5 μm). Ribbons long enough to form more than one loop (L_0 = 30 and 40 μm) had an inner loop with a radius $R_1 < R_0$ and an outer loop with radius $R_2 > R_0$. A ribbon with a length of 60 μm shape shifted into a helix with a radius R_h (3.9 μm) slightly greater

Table 1 Roll and helix (pH 3.0) radii (μm) [D_p = 0.5 fC]

	L_0	R_0	R_1	R_2	R_H
<Single loop roll	8	3.5			
	12	3.5			
Multi-loop roll	30		3.3	5.1	
	40		3.1	6.3	
Helix	60				3.9

than R_0 where the reduced bending energy per loop can offset the added shear energy due to the lateral displacement of each loop. The number of loops depends on the aspect ratio and the point dose. Increasing the point dose to 2 fC, for example, enables a ribbon with a length of 60 μm and width of 2 μm to remain in the roll conformation at pH 3.0 with three concentric loops (data not shown).

Despite the apparent spaces between successive turns of the helix in Fig. 3(D), this helix has a minimal pitch, *i.e.*, one that just satisfies the self-avoiding condition. As indicated by the Cy3 (red) contrast, the spacing between successive turns is ~500 nm. This distance corresponds closely to the critical separation indicated by Fig. 2. We note, however, that successive turns of this helix are not covalently connected to each other. They are separated by high-swelling gel created by proximity effects along the edges of the as-patterned rectangular ribbon. The actual spacing between them is determined by an energetic balance between the shear that generates the helix and compression of the proximity-effect gel between successive turns of the helix.

Modelling demonstrates similar trends in the shape-shifted ribbon morphology as a function of ribbon length (Fig. 3(E)–(G)). Short ribbons form an arc with a radius of R_0. Longer ribbons form a multi-loop roll with the radii of the inner loop, R_1, less than R_0 and the radius of the outer loop, R_2, greater than R_0. Still longer ribbons transform into helices with a helical radius, R_h, slightly greater than R_0. These simulations further show that, for a ribbon of sufficient length, the energetic differences between a helical conformation and a multiloop roll conformation are relatively small. These small differences likely enable the transition structure (Fig. 3(C)) that displays elements of both the roll and the helical conformations.

3.3.B Effect of electron dose. We have previously shown in e-beam patterned PAA lines that increasing the point dose increases the ratio of higher modulus to lower-modulus material in the through-thickness direction.[21] In those experiments, the line shape shifted into a helix, and the helical radius increased with increasing dose. We see a similar dependence of radius on dose here with ribbons. But, because of their lower length/width ratio, the ribbons transformed into rolls. For each dose, we patterned a series of ribbon lengths to identify the specific length that achieved one complete 2π turn (Fig. S4, ESI†). We then measured the roll radius as a function of the point dose used to pattern the ribbon. We again see that radius increases with increasing dose (Fig. 4).

In his classic work on the bending of bilayer plates due to differential thermal expansion,[12] Timoshenko showed that the bending curvature depends on the ratio of the individual layer thicknesses. Much more recently, Smela *et al.* have used the Timoshenko formulation to model the bending of polymer/Au bilayer ribbons where the polymer layer expanded or contracted depending on the oxidation conditions.[36] They found that the ribbon curvature increased with increasing polymer/Au thickness ratios up to a ratio of about 5 and could be modelled using the Timoshenko formula after corrections to accommodate through-thickness variations in the strain of the polymer layer.

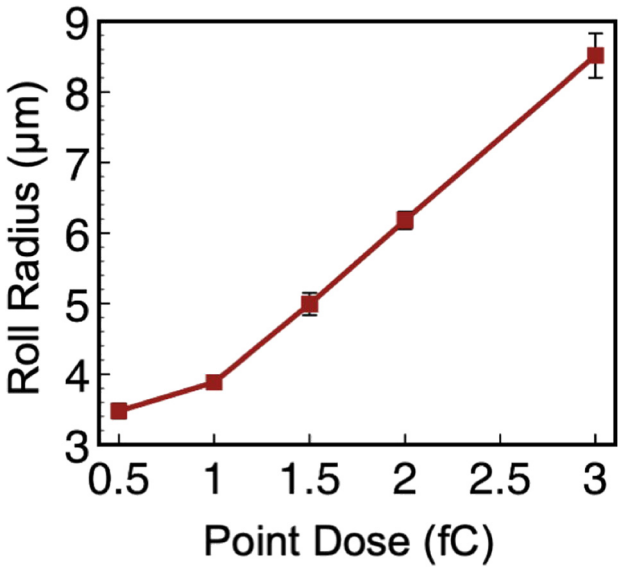

Fig. 4 The radius of a roll (pH 3.0) increases with increasing the point dose (D_p). The image data are presented in Fig. S4 (ESI†). Each data point and error bar represent the average and standard deviation, respectively, from measurements from n = 3 different single-loop roll structures.

In other words, bilayers with a larger fraction of the high-modulus Au would curl into rolls with a larger radius than those with a lower fraction of Au. In our ribbon geometry, the thickness of the high-swelling low-modulus material (region 3) is less than that of the non-swelling higher-modulus material (regions 1 and 2) (see Fig. 1(E)). The data in Fig. 4 indicate that the ribbons effectively become more rigid with increasing dose. This is a consequence of the shifting ratio of high-modulus to low-modulus material through the ribbon thickness. The total ribbon thickness is determined primarily by the incident electron energy, since, with all else equal, this energy determines the average electron range. The ribbon thickness depends only weakly on dose.[21] Increasing the dose increases the fraction of high-modulus material, so the ribbon becomes more rigid and the roll curvature consequently also increases. Such behavior is consistent with our dose-dependent radiation-chemistry model[21] and the Timoshenko bilayer-bending model.

3.3.C Mapping the shape-shifted morphology. Because it does not require a mask, e-beam lithography can rapidly pattern ribbons to explore how the shape-shifted morphology depends on such variables as the ribbon dimensions and the electron dose. Fig. 5 maps the shape-shifted morphology after a large number of patterns were developed and imaged in pH 3.0 buffer. It shows a number of things. The transition from a single-loop roll to a multi-loop roll requires longer ribbons as the patterning dose is increased. This is consistent with the data in Fig. 4 indicating that increasing dose increases the roll radius and, hence, the roll circumference. Similarly, the multi-loop roll is stabilized with increasing dose. At lower doses we see the transition from roll to helix with increasing ribbon aspect ratio. We note that the helices in this region of the morphology map all have a minimal pitch.

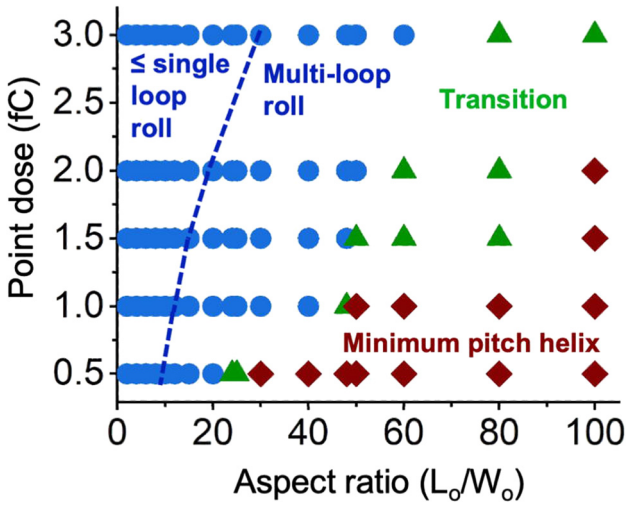

Fig. 5 The shape-shifted morphology depends on the point dose used during e-beam patterning and on the ribbon aspect ratio.

The chirality of the helical ribbons is random. Table 2 summarizes chirality results for two particular configurations studied in detail. These were patterned using a point dose of 0.5 fC and a ribbon width of 2 μm. Of the 39 ribbons patterned with an initial length of 60 μm, 18 were left handed while 21 were right handed. Their chirality did not change when the pH was increased from 3.0 to 7.4. Ribbons with L_0 = 40 μm have an aspect ratio of 20. The morphology map of Fig. 5 indicates that these ribbons form multi-loop rolls when developed and imaged in pH 3.0 buffer. These rolls are achiral. As discussed below (Section 3.4), when the pH is raised to 7.4, the rolls shape shift to form helices. Table 2 indicates that the chirality of these helices is again random with almost identical numbers of right-handed and left-handed helices.

3.4 pH-dependent elasto-plastic effects

PAA is a weak polyelectrolyte with a pK_a of about 5.[37,38] Raising the pH to 7.4 deprotonates the majority of PAA acid groups, and the region 3 gel material swells by orders of magnitude because of the Donnan effect.[33] As shown by Fig. 6(A1) and (A2), after developing in pH3 buffer (D3), this additional swelling at pH 7.4 produces substantially higher out-of-plane bending which in turn generates a much higher helical curvature. When the pH is returned to 3.0, however, the helix does not return to its original shape. Significantly, its pitch is no longer minimal.

We have mapped the shape-shifted morphology as a function of aspect ratio and dose after the various structures were developed at pH 3.0 and then exposed to pH 7.4. These results are summarized by Fig. S5 (ESI†). Not only do the minimal-pitch helices like those in Fig. 6 transform to nonminimal-pitch helices, but the transition structures and the multi-loop rolls observed at pH 3.0 also transform into nonminimal-pitch helices. Because of the higher bending, the loop radius decreases when a roll at pH 3.0 transforms into a helix at pH 7.4. Hence, a multi-loop helix can form at pH 7.4 from a roll that may not even complete a full loop at pH 3.0. There also remains a subset of ribbons with lower aspect ratios that are unable to complete a full loop at pH 7.0, and these form arcs. The longer of these arcs show signs of shear (see images in Fig. S5, ESI†) even though they do need form a complete loop and do not need to meet the self-avoiding condition.

Table 2 Ribbon chirality (D_p = 0.5 fC)

W_0 = 2 μm	L_0 = 40 μm		L_0 = 60 μm	
Chirality	Left	Right	Left	Right
pH 3.0	0	0	18	21
pH 7.4	21	20	18	21

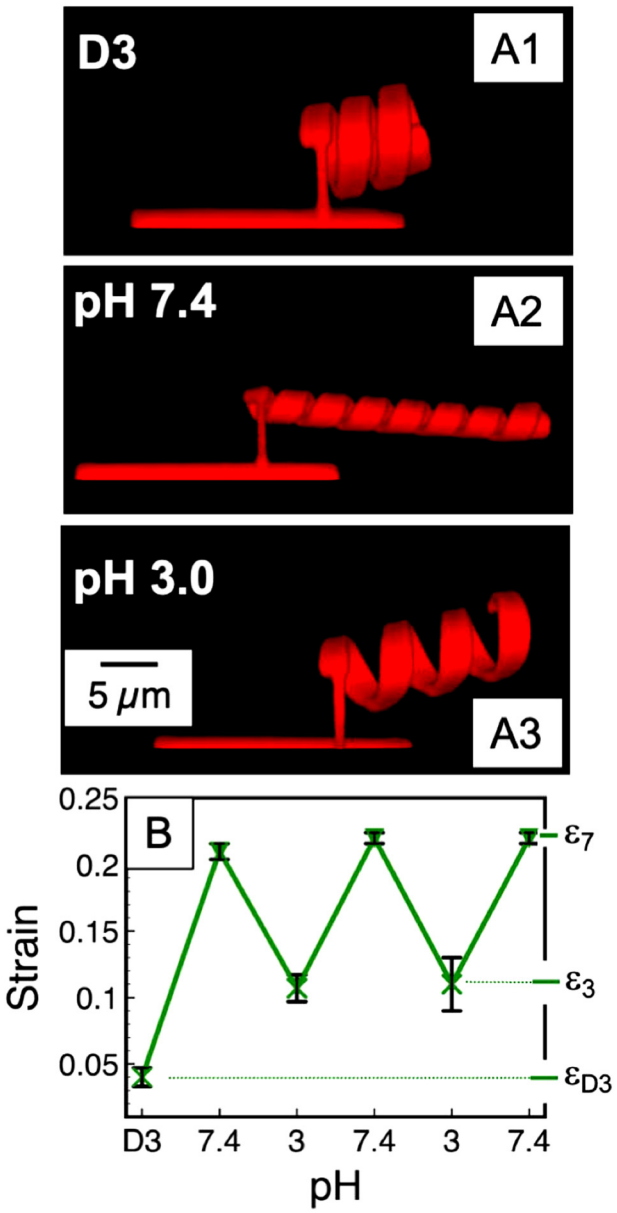

Fig. 6 Excursions in pH produce both plastic and elastic strain. A PAA ribbon (W_0 = 2 μm; L_0 = 60 μm; D_p = 0.5 fC) after: (A1) developing in pH 3.0 buffer [D3]; (A2) changing to pH 7.4 buffer; and (A3) changing back to pH 3.0 buffer. (B) The longitudinal strain depends on pH. The points and error bars correspond to the average and standard deviation, respectively, from 3 different ribbons.

A non-minimal pitch indicates that, in addition to the through-thickness swelling gradient that creates out-of-plane bending, an additional in-plane anisotropy is produced by the excursion to pH 7.4. In our case, the in-plane anisotropy is related to plastic deformation. Fig. 6(B) follows the ribbon's longitudinal strain, ε, defined as the extension in ribbon length ΔL normalized to its original length, L_0, while the pH was cycled between 3.0 and 7.4. The ribbon elongates by only a few percent (ε_{D3}) when the as-patterned structure is first developed in pH 3.0 buffer (D3). The strain increases to more than 20% (ε_7) at pH 7.4. When the pH is the lowered back to 3.0, the strain lowers to ε_3, but this strain value is higher than it was in the original pH 3.0 development buffer. While subsequent cycling between pH 7.4 and 3.0 generates a recoverable elastic strain ($\varepsilon_7 - \varepsilon_3$), there remains a plastic strain ($\varepsilon_3 - \varepsilon_{D3}$) which is not recovered.

Plastic deformation in amorphous crosslinked polymers can occur by the formation and propagation of shear bands.[39–41] These occur along directions of maximum shear which correspond to an angle approximately 45° from the direction of loading (the ribbon's long axis).[41] We speculate that shear bands form in the region 2 portion of the ribbon where the material is hydrophobic and has a crosslink density less than that of the region 1 material.[21] Within the shear bands, polymer segments between crosslinks align themselves along the direction of maximum shear and then generate a modulus both higher and misoriented relative to the surrounding undeformed material. Hence, shear bands generate an in-plane anisotropy of the elastic modulus which can account both for the plastic deformation and for the non-minimal pitch associated with it. In contrast, plastic deformation *via* crazing would not generate an in-plane anisotropy in a direction different from that already being produced by the out-of-plane swelling and would thus not produce a non-minimal helical pitch.

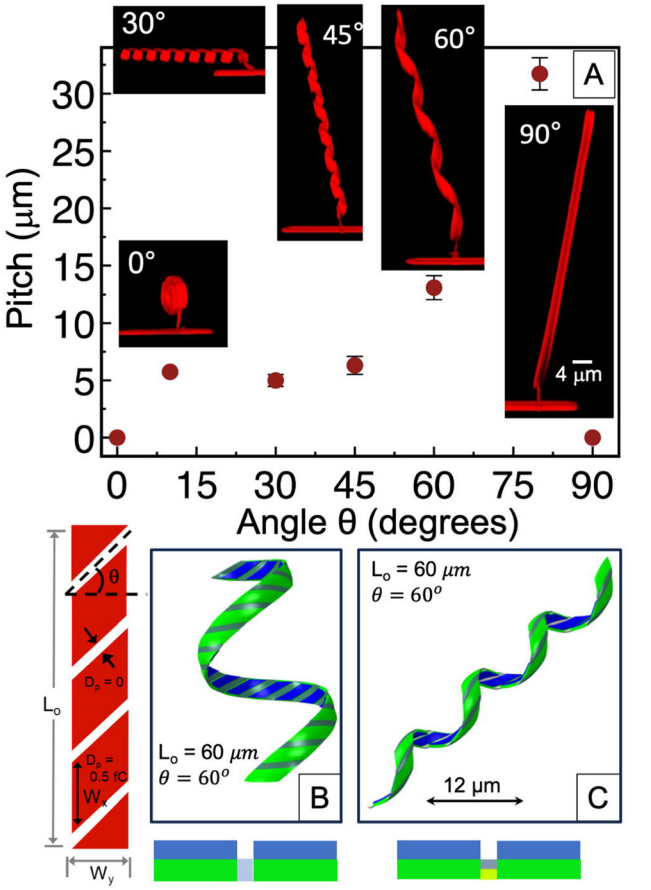

Fig. 7 (A) An in-plane anisotropy can be created by patterning parallelogram-shaped tiles offset from each other by a gap at an angle θ. Varying θ changes the ribbon from a roll (0°), to a non-minimal pitch helix (10°–80°), to a tube (90°). Patterning parameters: W_y = 2 μm; L_0 = 60 μm; gap distance = 500 nm; D_p = 0.5 fC; pH = 3.0. Modelling (θ = 60°; L_0 = 60 μm) where the gap material is assumed to be (B) homogeneous with a low modulus; and (C) have a through-thickness swelling gradient.

3.6 Tiled ribbons with patterned in-plane anisotropy

If the ribbons remain in the initial pH 3.0 development buffer, we avoid the plastic deformation that creates the in-plane anisotropy. We can, however, intentionally pattern an in-plane anisotropy. The schematic in Fig. 7 outlines one such pattern. Parallelogram-shaped tiles were patterned using a point dose of 0.5 fC, and these were offset from each other by a gap of 500 nm where no patterning was done. Electron exposure in the gap regions was due entirely to proximity effects from patterning the adjacent tiles. Since the gap dimension was less than 550 nm, the tiles remain covalently connected to form a ribbon. The centerline within each gap corresponds to a gel-like with an elastic modulus much lower than the adjacent patterned tiles. This anisotropy is opposite to the effect of shear-band formation where the modulus would locally increase.

Lithography can pattern the in-plane anisotropy at precise and prescribed angles relative to ribbon axis. Fig. 7 maps the shape-shifted morphology as a function of the gap angle. At θ = 0° the gaps are aligned perpendicular to the ribbon's long axis. This alignment produces no new torque on the ribbon, and the ribbon shape shifts into a roll somewhat akin to a continuous ribbon with no gaps (Fig. 3(B)). At θ = 90° the gaps are parallel to the ribbon axes, and they run the entire length of the ribbon. This orientation again produces no additional torque, and the ribbon shape shifts into a tube-like structure. In between these extremes, the ribbons shape shift into non-minimal-pitch helices with a pitch determined by the gap angle θ. These same trends have been reported by Chen *et al.*[19] for the case of high-modulus wires embedded at controlled angles in pre-stressed elastomeric ribbons with characteristic dimensions of centimeters. In contrast, our structures are patterned in the ~1–100 μm range with much higher aspect ratios.

We initially anticipated that this patterning procedure would mimic experiments such as those with embedded wires having a different modulus than the surrounding material. However, in our case, modelling indicates that the dominant mechanism controlling the helical morphology in these tiled ribbons is not the in-plane anisotropy of the elastic modulus of the gap material. Instead, the shape shifting is dominated by the swelling gradient of the gap material along the through-thickness

direction. Fig. 7(B) illustrates one example where the gap material (θ = 60°) was assumed to be homogeneous. To minimize the computational burden of discretizing too many elements and using a very small simulation timestep, we modelled the gap material with an assumed thickness of 200 nm and a modulus of 0.1 MPa rather than the measured thickness (~20 nm) and the modulus of 1 MPa assumed for the region 3 material. Fig. 7(C) addresses an identical tiled ribbon except that the gap material was assumed to have a though-thickness swelling gradient. That gradient was approximated by a bilayer structure with a non-swelling top layer and a swelling bottom layer. The extent of swelling was determined by recapitulating the tilt angle between adjacent tiles in the tile-separation experiment (Fig. 2(B)). It should be highlighted that the gap thickness, moduli, and the swelling ratios are only fitting parameters to capture the gap dominated shape changes, which are not unique. The predicted helical morphology in this latter case (Fig. 7(C)) is much more consistent with the corresponding experimental result, notably in terms of the pitch and helical radius. The model thus suggests that the shape shifting corresponds more closely to an origami mechanism with foldable hinges and stiff panels.[42,43]

Irrespective of the mechanism driving the shape shifting, we note that the helical chirality is completely controlled by the gap orientation. The helices shown in Fig. 7 with gap angles of $10° \leq \theta \leq 80°$ have a chirality that is everywhere left-handed. Fig. S6 (ESI†) shows images of tiled ribbons for which θ = 45° and θ = 135°. The resulting helices are identical except that their chirality is opposite. We patterned 24 different tiled ribbons with various gap orientations in the range of $100° \leq \theta \leq 170°$. Every one of the resulting helices had a right-handed chirality. These chirality-control data are summarized in tables associated with Fig. S6 (ESI†).

4. Conclusions

For the study of ribbons with through-thickness and in-plane anisotropies, electron-beam lithography accesses some processing attributes unavailable to the more commonly used methods of photolithography and mechanical bilayer fabrication. Among these is the ability to pattern homopolymer films without the need for initiators, crosslinking agents, or adhesives. The radiation chemistry alone can drive crosslinking. The extent of crosslinking can furthermore be controlled *via* the incident electron dose, which, like the patterning geometry itself, can be easily varied through the digital inputs that drive the lithography.

We exploited these characteristics to pattern thin ribbons with widths on the order of a few microns and lengths ranging from ~5–100 μm in pure poly(acrylic acid). Because of the depth-dependent adsorption of the electron energy, these ribbons have a through-thickness gradient in structure. Material near the incident (top) surface is heavily crosslinked and hydrophobic. Material near the bottom surface is lightly crosslinked and behaves as a pH-sensitive polyelectrolyte gel. Swelling of this gel layer drives out-of-plane bending. The patterning was done so that, upon development in a good solvent for homopolymer PAA, the ribbons could reconfigure themselves into an equilibrium morphology. That morphology – a single-loop roll, a multi-loop role, or a minimal-pitch helix – could be prescribed based on the ribbon aspect ratio and the incident electron dose. The fact that PAA is a weak polyelectrolyte enabled the swelling stress to be substantially increased when the pH was raised from below to above the PAA pK_a (~5). The dominant morphology at pH 7.4 corresponded to helices. Furthermore, the helical pitch changed from minimal to non-minimal because of the development of in-plane mechanical anisotropies associated with plastic deformation. Mimicking that in-plane anisotropy by patterning tiled ribbons again enabled control over the shape-shifted morphology. The shape-shifting mechanism, however, was more akin to that associated with rigid origami where bending of the gap material between adjacent tiles dominates over the in-plane mechanical anisotropies introduced by the gaps. This latter observation opens possibilities for the future exploration of origami-based structures in a range of homopolymer systems at micron length scales.

Author contributions

X. W. and M. L. designed the experiments. X. W. performed the experiments. T. Z. performed finite element modelling. X. W. and M. L. did the primary writing. All authors participated in the review and editing. M. L. was responsible for funding acquisition and project administration.

Data availability

The data supporting this article have been included as part of the ESI.†

Conflicts of interest

There are no conflicts to declare.

Acknowledgements

This project was supported at Stevens by the Army Research Office *via* grant number W911NF2010277. Work at Syracuse was supported by the National Science Foundation *via* grant number NSF-CMMI-2022421.

Notes and references

1 M. S. Sousa-Baena, J. Hernandes-Lopes and M. A. Van Sluys, Reaching the top through a tortuous path: helical growth in climbing plants, *Curr. Opin. Plant Biol.*, 2021, **59**, 101982, DOI: 10.1016/j.pbi.2020.101982.

2 P. Ball, In retrospect: On Growth and Form, *Nature*, 2013, **494**(7435), 32–33, DOI: 10.1038/494032a.

3 D. A. W. Thompson, *On Growth and Form*, University Press, 1917.
4 K. A. Dill and J. L. MacCallum, The protein-folding problem, 50 years on, *Science*, 2012, **338**(6110), 1042–1046, DOI: 10.1126/science.1219021.
5 L. Pauling and R. B. Corey, Configuration of polypeptide chains, *Nature*, 1951, **168**(4274), 550–551, DOI: 10.1038/168550a0.
6 E. Yashima, N. Ousaka, D. Taura, K. Shimomura, T. Ikai and K. Maeda, Supramolecular Helical Systems: Helical Assemblies of Small Molecules, Foldamers, and Polymers with Chiral Amplification and Their Functions, *Chem. Rev.*, 2016, **116**(22), 13752–13990, DOI: 10.1021/acs.chemrev.6b00354.
7 G. Huang and Y. Mei, Helices in micro-world: Materials, properties, and applications, *J. Materiomics*, 2015, **1**(4), 296–306, DOI: 10.1016/j.jmat.2015.09.002.
8 G. M. Spinks, Advanced Actuator Materials Powered by Biomimetic Helical Fiber Topologies, *Adv. Mater.*, 2020, **32**(18), 1904093, DOI: 10.1002/adma.201904093.
9 T. van Manen, S. Janbaz and A. A. Zadpoor, Programming the shape-shifting of flat soft matter, *Mater. Today*, 2018, **21**(2), 144–163, DOI: 10.1016/j.mattod.2017.08.026.
10 J. Zhou and S. S. Sheiko, Reversible shape-shifting in polymeric materials, *J. Polym. Sci., Part B: Polym. Phys.*, 2016, **54**(14), 1365–1380, DOI: 10.1002/polb.24014.
11 D. Sobel Longitude: the true story of a lone genius who solved the greatest scientific problem of his time, Fourth Estate, 1996.
12 S. Timoshenko, Analysis of Bi-Metal Thermostats, *J. Opt. Soc. Am.*, 1925, **11**(3), 233–255, DOI: 10.1364/JOSA.11.000233.
13 S. Armon, E. Efrati, R. Kupferman and E. Sharon, Geometry and Mechanics in the Opening of Chiral Seed Pods, *Science*, 2011, **333**(6050), 1726–1730, DOI: 10.1126/science.1203874.
14 Z. Chen, Q. Guo, C. Majidi, W. Chen, D. J. Srolovitz and M. P. Haataja, Nonlinear geometric effects in mechanical bistable morphing structures, *Phys. Rev. Lett.*, 2012, **109**(11), 114302, DOI: 10.1103/PhysRevLett.109.114302.
15 J. Huang, J. Liu, B. Kroll, K. Bertoldi and D. R. Clarke, Spontaneous and deterministic three-dimensional curling of pre-strained elastomeric bi-strips, *Soft Matter*, 2012, **8**(23), 6291–6300, DOI: 10.1039/c2sm25278c.
16 M. Huang, C. Boons, M. Roberts, D. E. Savage, M. G. Lagally, N. Shaji, H. Qin, R. Blick, J. A. Nairn and F. Liu, Nanomechanical architecture of strained bilayer thin films: From design principles to experimental fabrication, *Adv. Mater.*, 2005, **17**(23), 2860–2864, DOI: 10.1002/adma.200501353.
17 Y. Zhou, C. M. Duque, C. D. Santangelo and R. C. Hayward, Biasing Buckling Direction in Shape-Programmable Hydrogel Sheets with Through-Thickness Gradients, *Adv. Funct. Mater.*, 2019, **29**(48), 1905273, DOI: 10.1002/adfm.201905273.
18 Z. L. Wu, M. Moshe, J. Greener, H. Therien-Aubin, Z. Nie, E. Sharon and E. Kumacheva, Three-dimensional shape transformations of hydrogel sheets induced by small-scale modulation of internal stresses, *Nat. Commun.*, 2013, **4**, 1586, DOI: 10.1038/ncomms2549.
19 X. Yu, L. Zhang, N. Hu, H. Grover, S. Huang, D. Wang and Z. Chen, Shape formation of helical ribbons induced by material anisotropy, *Appl. Phys. Lett.*, 2017, **110**(9), 091901, DOI: 10.1063/1.4977090.
20 S. J. Jeon, A. W. Hauser and R. C. Hayward, Shape-Morphing Materials from Stimuli-Responsive Hydrogel Hybrids, *Acc. Chem. Res.*, 2017, **50**(2), 161–169, DOI: 10.1021/acs.accounts.6b00570.
21 X. Wu, F. Teng, E. Firlar, T. Zhang and M. Libera, Elasto-Plastic Effects on Shape-Shifting Electron-Beam-Patterned Gel-Based Micro-Helices, *Mater. Horiz.*, 2024, **11**, 3427–3436, DOI: 10.1039/D4MH00208C.
22 A. Singh, A. Shi and S. A. Claridge, Nanometer-scale patterning of hard and soft interfaces: from photolithography to molecular-scale design, *Chem. Commun.*, 2022, **58**(94), 13059–13070, DOI: 10.1039/d2cc05221k.
23 C. Con, R. Dey, M. Ferguson, J. Zhang, R. Mansour, M. Yavuz and B. Cui, High molecular weight polystyrene as very sensitive electron beam resist, *Microelectron. Eng.*, 2012, **98**, 254–257, DOI: 10.1016/j.mee.2012.07.005.
24 K. L. Christman, E. Schopf, R. M. Broyer, R. C. Li, Y. Chen and H. D. Maynard, Positioning multiple proteins at the nanoscale with electron beam cross-linked functional polymers, *J. Am. Chem. Soc.*, 2009, **131**(2), 521–527, DOI: 10.1021/ja804767j.
25 P. Krsko, S. Sukhishvili, M. Mansfield, R. Clancy and M. Libera, Electron-beam surface-patterned poly(ethylene glycol) microhydrogels, *Langmuir*, 2003, **19**(14), 5618–5625, DOI: 10.1021/la034157r.
26 C. M. Kolodziej and H. D. Maynard, Electron-beam lithography for patterning biomolecules at the micron and nanometer scale, *Chem. Mater.*, 2012, **24**(5), 774–780, DOI: 10.1021/cm202669f.
27 I. Saaem and J. Tian, e-Beam nanopatterned photoresponsive bacteriorhodopsin-containing hydrogels, *Adv. Mater.*, 2007, **19**(23), 4268–4271, DOI: 10.1002/adma.200701401.
28 R. F. Egerton, Electron energy-loss spectroscopy in the TEM, *Rep. Prog. Phys.*, 2009, **72**(1), 016502, DOI: 10.1088/0034-4885/72/1/016502.
29 C. L. Moad and D. J. Winzor, Quantitative characterization of radiation degradation in polymers by evaluation of scission and cross-linking yields, *Prog. Polym. Sci.*, 1998, 759–813, DOI: 10.1016/s0079-6700(97)00041-5.
30 D. J. T. Hill, J. H. O'Donnell, C. L. Winzor and D. J. Winzor, Evaluation of scission and crosslinking yields in γ-irradiated poly(acrylic acid) and poly(methacrylic acid) from weight- and *Z*-average molecular weights determined by sedimentation equilibrium, *Polymer*, 1990, **31**(3), 538–542, DOI: 10.1016/0032-3861(90)90399-J.
31 D. C. Joy, *Monte Carlo Modeling for Electron Microscopy and Microanalysis*, Oxford University Press, 1995.
32 R. Shimizu and D. Ze-Jun, Monte Carlo modelling of electron-solid interactions, *Rep. Prog. Phys.*, 1992, 487–531.
33 D. Jia and M. Muthukumar, Theory of Charged Gels: Swelling, Elasticity, and Dynamics, *Gels*, 2021, **7**(2), 49, DOI: 10.3390/gels7020049.
34 M. McCord and M. Rooks, Electron Beam Lithography, in *Handbook of Microlithography*, ed. Rai-Choudhury, SPIE, 1997.

35 P. Li, A review of proximity effect correction in electron-beam lithography, *arXiv*, 2015, preprint, arXiv:1509.05169, DOI: 10.48550/arXiv.1509.05169.
36 M. Christophersen, B. Shapiro and E. Smela, Characterization and modeling of PPy bilayer microactuators. Part 1. Curvature, *Sens. Actuators, B*, 2006, **115**(2), 596–609, DOI: 10.1016/j.snb.2005.10.023.
37 T. Swift, L. Swanson, M. Geoghegan and S. Rimmer, The pH-responsive behaviour of poly(acrylic acid) in aqueous solution is dependent on molar mass, *Soft Matter*, 2016, **12**(9), 2542–2549, DOI: 10.1039/C5SM02693H.
38 X. Xiao, J. Ji, W. Zhou, S. Nanjia and M. Libera, Salt Destabilization of Cationic Colistin Complexation within Polyanionic Microgels, *Macromolecules*, 2022, **55**(5), 1736–1746, DOI: 10.1021/acs.macromol.1c02157.
39 A. M. Donald and E. J. Kramer, The competition between shear deformation and crazing in glassy polymers, *J. Mater. Sci.*, 1982, **17**(7), 1871–1879, DOI: 10.1007/BF00540402.
40 R. N. Haward, *The Physics of Glassy Polymers*, Wiley, 1973.
41 I. M. Ward and J. Sweeney, *Mechanical Properties of Solid Polymers*, Wiley, 2013.
42 Z. Chen, Y. Li and Q. M. Li, Hydrogel-driven origami metamaterials for tunable swelling behavior, *Mater. Des.*, 2021, **207**, 109819, DOI: 10.1016/j.matdes.2021.109819.
43 C. Lv, D. Krishnaraju, G. Konjevod, H. Yu and H. Jiang, Origami based mechanical metamaterials, *Sci. Rep.*, 2014, **4**(1), 5979, DOI: 10.1038/srep05979.

